

# Testing the weak equivalence principle by differential measurements of fundamental constants in the Magellanic Clouds

S. A. Levshakov<sup>1,2\*</sup>, K.-W. Ng<sup>3,4</sup>, C. Henkel<sup>5,6</sup>, B. Mookerjee<sup>7</sup>, I. I. Agafonova<sup>2</sup>, S.-Y. Liu<sup>4</sup> and W.-H. Wang<sup>4</sup>

<sup>1</sup>*Ioffe Physical-Technical Institute, 194021 St. Petersburg, Russia*

<sup>2</sup>*Electrotechnical University “LETI”, 197376 St. Petersburg, Russia*

<sup>3</sup>*Institute of Physics, Academia Sinica, Taipei 11529, Taiwan*

<sup>4</sup>*Institute of Astronomy and Astrophysics, Academia Sinica, Taipei 11529, Taiwan*

<sup>5</sup>*Max Planck Institut für Radioastronomie, Auf dem Hügel 69, 53121 Bonn, Germany*

<sup>6</sup>*Astron. Dept., King Abdulaziz University, PO Box 80203, 21589 Jeddah, Saudi Arabia*

<sup>7</sup>*Tata Institute of Fundamental Research, Homi Bhabha Road, 400005 Mumbai, India*

Accepted XXX. Received YYY; in original form ZZZ

## ABSTRACT

Non-standard fields are assumed to be responsible for phenomena attributed to dark energy and dark matter. Being coupled to ordinary matter, these fields modify the masses and/or charges of the elementary particles, thereby violating the Weak Equivalence Principle. Thus, values of fundamental constants such as the proton-to-electron mass ratio,  $\mu$ , and/or the fine structure constant,  $\alpha$ , measured in different environment conditions can be used as probes for this coupling. Here we perform differential measurements of  $F = \mu\alpha^2$  to test a non-standard coupling in the Magellanic Clouds – dwarf galaxies where the overall mass budget is dominated by dark matter. The analysis is based on [C I] and CO lines observed with the *Herschel Space Observatory*. Since these lines have different sensitivities to changes in  $\mu$  and  $\alpha$ , the combined  $\alpha$  and  $\mu$  variations can be evaluated through the radial velocity offsets,  $\Delta V$ , between the CO and [C I] lines. Averaging over nine positions in the Magellanic Clouds, we obtain  $\langle \Delta V \rangle = -0.02 \pm 0.07$  km s<sup>-1</sup>, leading to  $|\Delta F/F| < 2 \times 10^{-7}$  ( $1\sigma$ ), where  $\Delta F/F = (F_{\text{obs}} - F_{\text{lab}})/F_{\text{lab}}$ . However, for one position observed with five times higher spectral resolution we find  $\Delta V = -0.05 \pm 0.02$  km s<sup>-1</sup>, resulting in  $\Delta F/F = (-1.7 \pm 0.7) \times 10^{-7}$ . Whether this offset is due to changes in the fundamental constants, due to chemical segregation in the emitting gas or merely due to Doppler noise requires further investigations.

**Key words:** methods: observational – techniques: spectroscopic – galaxies: Magellanic Clouds – radio lines: ISM – elementary particles – dark matter

## 1 INTRODUCTION

The weak equivalence principle (WEP) is one of the basic postulates of Einstein’s general relativity (GR). It assumes the equality of the inertial and gravitational mass, or, in terms of the field theory, the universal and minimal coupling of all matter fields to a single metric. Up to now, GR (and, hence, WEP) successfully withstands all possible tests including those performed under extreme gravity (e.g., Archibald et al. 2018; Will 2014). However, it is widely be-

lieved that  $\sim 95\%$  of the energy density of the Universe is concentrated in the so called ‘dark sector’ comprising the non-baryonic dark matter (DM,  $\sim 26\%$ ) used to explain the CMB spectrum, the formation of the large-scale structure and the observed discrepancy between visible and dynamical masses in galaxies and clusters, and the dark energy (DE,  $\sim 69\%$ ) responsible for the cosmic acceleration at low redshifts ( $z < 1$ ). Both these substances cannot be understood within the framework of GR and the Standard Model of particle physics.

To explain the cosmic acceleration either new scalar fields are explicitly introduced, or the Einstein field equa-

\* E-mail: lev@astro.ioffe.ru

tions are modified what effectively is equivalent to the introduction of additional fields (Brax 2018; Nojiri et al. 2017; Joyce et al. 2016). Some models allow these fields to couple to baryonic matter. As for the DM, the paradigm for most favorable candidates shifts now from weakly interacting massive ( $m \sim \text{GeV}$ ) particles (WIMPs) to light or ultra-light ( $m \sim 10^{-3}$  eV down to  $\sim 10^{-22}$  eV) axion-like particles (ALPs) (Hui et al. 2017; Berezhiani & Khoury 2015; Feng 2010). The main difference between the WIMPs and ALPs is that WIMPs are collisionless and interact only via gravitation, whereas ALPs are self-interacting, behave under special conditions as a quantum liquid and can fundamentally couple to ordinary matter (Irastorza & Redondo 2018).

Additional coupling – being dependent on space, time and/or chemical composition – would break the condition of universal coupling to the metric, thereby violating the WEP. Since detection of any violation of the WEP would manifest the presence of an unknown interaction and, hence, a new physics beyond the Standard Model, various laboratory and satellite experiments were carried out aimed at testing the WEP with highest precision possible. Up to now, nowhere any signal over the background was found (Bergé et al. 2018; Antoniou & Perivolaropoulos 2017; Rider et al. 2016; Brax & Davis 2016; Li et al. 2016; Hamilton et al. 2015; Wagner et al. 2012).

One thing to notice is that if the anticipated new fields are so light as considered in theory, then their gradients (fifth force) would be detectable only at scales of an order of (inter)galactic distances. Another reason for null results could be a screening (damping) of these fields in the environments where the experiments were performed. Several screening mechanisms were proposed and widely discussed in the literature, e.g. a popular chameleon field model suggested by Khoury & Weltman (2004), when coupling strength depends on the environmental matter density, or a concept of emergent gravity recently developed by Verlinde (2017), where additional coupling is modulated by surface mass density of baryons. However, none of these screening models has yet been verified experimentally.

In such a case it seems natural to search for a new field-baryon coupling just in places where the presence of non-standard fields could be supposed from the phenomenology. In this respect the position of the Sun in the Milky Way (MW) is not very favorable: different approaches to modeling the MW rotational curve come to the same conclusion that the total matter within the solar circle is dominated by baryons with  $\rho_b/\rho_{\text{DM}} \sim 10$ , where  $\rho_b$  is the baryon density and  $\rho_{\text{DM}}$  is the density of DM (McGaugh 2018; McMillan 2017; Iocco et al. 2015; Sofue et al. 2009). On the other hand, the effects attributed to DM become prominent either at outskirts of massive galaxies or in dwarf galaxies where a significant discrepancy between the visible and dynamical masses is observed. Thus, to catch a glimpse of new field(s) the targets should be selected either far from galactic centres or in dwarfs.

In the present work, we search for a new field-induced coupling in molecular clouds within the Large and Small Magellanic Clouds (LMC and SMC). Both of them are bright dwarfs detached from the solar system by  $\sim 50$  kpc and  $\sim 60$  kpc, respectively. In the SMC, the DM component is believed to dominate the overall mass budget at all distances from the centre,  $\rho_b/\rho_{\text{DM}} < 0.5$  (Di Teodoro et

al. 2019). In the LMC, the contribution of the DM halo is not well constrained because of complex kinematics of stars and gas which prevents the detailed rotation curve decomposition (Vasiliev 2018; van der Marel & Kallivayalil 2014), but at galactocentric distances  $R > 3$  kpc the input of DM definitely becomes significant,  $\rho_b/\rho_{\text{DM}} < 1$  (Buckley et al. 2015).

If new fields do exist and couple to the standard matter, then the fundamental coupling constants, primarily the proton-to-electron mass ratio  $\mu = m_p/m_e$  and possibly the fine structure constant  $\alpha = e^2/\hbar c$ , are predicted to vary (for a review, see, e.g., Safronova et al. 2018; Kozlov et al. 2018; Brax 2014; Uzan 2011). There are many atomic and molecular transitions which are highly sensitive to small changes in  $\mu$  and  $\alpha$  or in their combinations (Kozlov & Levshakov 2013), i.e., relative offsets in the transition frequencies induced by alleged changes in  $\mu$  and/or  $\alpha$  are large enough to be measured by spectroscopic methods which provide an unprecedented precision.

As yet, spectroscopy – both at optical and radio bands – was used to probe the time and space dependence of  $\mu$  and  $\alpha$  or their combinations both for cosmological and local objects (e.g., Ubachs 2018; Kanekar et al. 2018; Gupta et al. 2018; Levshakov et al. 2017). Up to now, the most stringent limits on fractional change in  $\mu$ ,  $\Delta\mu/\mu = (\mu_{\text{obs}} - \mu_{\text{lab}})/\mu_{\text{lab}}$ , and in  $\alpha$ ,  $\Delta\alpha/\alpha = (\alpha_{\text{obs}} - \alpha_{\text{lab}})/\alpha_{\text{lab}}$ , are as follows:  $\Delta\mu/\mu = (-3.0 \pm 6.0) \times 10^{-8}$  in one absorption-line system at  $z = 0.89$  (Kanekar et al. 2015; Marshall et al. 2017);  $\Delta\mu/\mu = (-3.5 \pm 1.2) \times 10^{-7}$  in one absorber at  $z = 0.69$  (Kanekar 2011);  $\Delta\mu/\mu = (-3.3 \pm 1.9) \times 10^{-8}$  in the dark cloud core L1498 in the MW disk (Daprà et al. 2017);  $\Delta\mu/\mu = (-2.0 \pm 1.0) \times 10^{-8}$  averaged over dark cloud cores in the MW disk within 300 pc from the Sun (Levshakov et al. 2010a,c, 2013). As for  $\alpha$ -variations, they were constrained at a much less sensitive limit:  $\Delta\alpha/\alpha = (0.1 \pm 1.7) \times 10^{-6}$  (Quast et al. 2004) and  $\Delta\alpha/\alpha = (-0.1 \pm 0.8) \times 10^{-6}$  (Levshakov et al. 2006) at  $z = 1.15$ ;  $\Delta\alpha/\alpha = (-1.5 \pm 2.6) \times 10^{-6}$  at  $z = 1.58$  (Agafonova et al. 2011);  $\Delta\alpha/\alpha = (1.3 \pm 2.4) \times 10^{-6}$  at  $z = 1.69$  (Molaro et al. 2013);  $\Delta\alpha/\alpha = (-1.4 \pm 0.9) \times 10^{-6}$  at  $z = 1.15$  (Kotuš et al. 2017);  $\Delta\alpha/\alpha = (3.3 \pm 2.9) \times 10^{-6}$  at  $z = 1.84$  (Bainbridge & Webb 2017). All estimates are given at  $1\sigma$  statistical significance.

These numbers show that competitive estimates of  $\Delta\mu/\mu$  and  $\Delta\alpha/\alpha$  should be at the level of a few  $10^{-7}$  which requires observations with a high spectral resolution and a high signal-to-noise (S/N) ratio. In this sense the best currently available data are the observations of the molecular clouds in the LMC and the SMC performed by the *Herschel Space Observatory*<sup>1</sup>.

As trial transitions we chose the rotational emission lines of CO, and the fine structure (FS) emission lines of [C I] and [C II]. The use of a combination of molecular rotational and atomic fine structure transitions to test the variability of the fundamental physical constants was first suggested by Levshakov et al. (2008). This approach being applied to constrain  $\mu$ - and/or  $\alpha$ -variations in Galactic and extragalactic objects has proved itself as a powerful tool for

<sup>1</sup> *Herschel* is an ESA space observatory with science instruments provided by European-led Principal Investigator consortia and with important participation from NASA.

probing the stability of the fundamental constants with an accuracy widely exceeded that of optical spectral measurements (Levshakov et al. 2010b, 2017). Another advantage of the [C I], [C II], and CO lines is that they are the most abundant species observed both in local and high redshift molecular systems and, hence, are convenient to make primary estimations and to select perspective targets.

## 2 METHOD

The frequencies of the rotational lines of light molecules are independent of  $\alpha$ , but sensitive to  $\mu$ , whereas the fine structure transition frequencies are proportional to  $\alpha^2$  and independent of  $\mu$ . Thus, comparing the observed frequencies of rotational and fine structure lines we estimate the value of  $\Delta F/F$  with  $F = \mu\alpha^2$  and  $\mu = m_p/m_e$  (Levshakov et al. 2008, 2010b). Converting the frequency scale,  $\nu$ , into the velocity scale,  $V$ , by

$$V/c = 1 - \nu_{\text{obs}}/\nu_{\text{lab}}, \quad (1)$$

at  $V \ll c$ , the fractional change  $\Delta F/F$  is calculated as:

$$\Delta F/F = \Delta\mu/\mu + 2\Delta\alpha/\alpha = \Delta V/c, \quad (2)$$

where  $\Delta V = V_{\text{rot}} - V_{\text{fs}}$  is the difference between the radial velocities of the CO rotational line and the [C I] or [C II] FS line, and the radial velocity is the velocity of the line centre related to the observed and laboratory frequencies,  $\nu_{\text{obs}}$  and  $\nu_{\text{lab}}$ .

The line centre is determined through the fitting of a set of Gaussian components to the observed line. If the line is symmetric (one component profile), the line centre is simply a fitting parameter and its statistical error  $\sigma_{\text{stat}}$  is calculated by the standard procedure employing the covariance matrix.

If, however, the line is asymmetric (multicomponent profile), then its centre is defined as a point where the first order derivative of the fitting curve is equal to zero. Employing a common approach (e.g., Savitzky & Golay 1964), we draw a parabola through three points  $\{x_1, y_1; x_2, y_2; x_3, y_3\}$  of the fitting curve  $y(x)$  which include the intensity peak, and calculate the line centre  $x_0$  and its error  $\sigma_{\text{stat}}$  as

$$x_0 = \frac{x_1 + x_2}{2} - \frac{(y_2 - y_1)\Delta_{\text{ch}}}{y_1 - 2y_2 + y_3}, \quad (3)$$

and

$$\sigma_{\text{stat}} = \frac{\sigma_{\text{rms}} \cdot \Delta_{\text{ch}}}{(y_1 - 2y_2 + y_3)^2} \sqrt{(y_3 - y_2)^2 + (y_1 - y_3)^2 + (y_2 - y_1)^2},$$

where  $\sigma_{\text{rms}}$  is the average noise of a given spectrum, and the channel width  $\Delta_{\text{ch}} = x_2 - x_1 = x_3 - x_2$ .

Under real conditions the spatial distributions of different species do not trace each other exactly. This leads to additional velocity shifts between the line centres due to different kinematics of the emitting regions – the so-called Doppler noise (DN). In a single measurement, the DN may either mimic or obliterate a sought-for signal in  $\Delta F/F$ . However, the DN is supposed to be random and normally distributed, i.e., it has a zero mean and a finite variance, and, thus, it can be significantly reduced by averaging over a set of measurements.

## 3 DATA

We use deep observations of fine structure transitions of [C I]  $^3\text{P}_2 - ^3\text{P}_1$  (herein [C I]), [C II]  $^2\text{P}_{3/2} - ^2\text{P}_{1/2}$  and the  $J=7-6$  rotational transition of CO towards LMC and SMC. These observations were performed with the high resolution Heterodyne Instrument in the Far Infrared (HIFI) (de Graauw et al. 2010) on board the *Herschel Space Observatory* (Pilbratt et al. 2010). This data is complemented with observations of the  $J=1-0$  and  $J=3-2$  transitions of  $^{12}\text{CO}$  and  $^{13}\text{CO}$  from the ATNF Mopra<sup>2</sup> and APEX<sup>3</sup> telescopes respectively. We have retrieved the final reduced *User Provided Data Product* from the Herschel archive for the purpose of our analysis. The full description of observational data used in the present work is given by Pineda et al. (2017).

The baseline for each spectrum was defined by selecting spectral windows without emission lines and/or noise spikes and then calculating the mean main beam brightness temperature  $T_{\text{mb}}$  along with its rms uncertainty  $\sigma$  for each spectral window. Using spline interpolation through this set of pairs  $\{T_i, \sigma_i\}$  we obtained a baseline which was subtracted from the spectrum. Since the rms uncertainties  $\sigma_i$  are approximately identical for all windows, their mean value  $\sigma_{\text{rms}}$  was assigned to the whole spectrum.

Table 1 summarizes for all spectral lines considered here the laboratory frequencies and their uncertainties taken from the papers cited in the last column, the corresponding systematic errors in velocity ( $\sigma_{\text{sys}}$ ), and the beamsizes of the observations. The spectral lines are analyzed at different spectral resolutions which are given in Table 2 and indicated in Figs. 1-9. The errors  $\sigma_{\text{sys}}$  determine the limiting precision with which the line centres can be measured. In particular,  $\sigma(\Delta F/F)_{\text{lim}} = 2 \times 10^{-8}$  for the pair [C I]/CO(7-6).

## 4 RESULTS AND DISCUSSION

The measured lines centres,  $V_{\text{LSR}}$ , and their  $1\sigma$  statistical errors are listed in Table 2. Figures 1-9 show the observed spectra (dots with  $1\sigma$  error bars) and model curves (red solid lines) obtained by the fitting procedure.

In order to analyze a homogeneous sample we combine the 1.11 km  $\text{s}^{-1}$  channel width data (index “b” in Table 2), while the PDR3-NE 0.19 km  $\text{s}^{-1}$  channel width data (index “c” in Table 2) are considered separately. Since the sample size is small,  $n = 9$ , the Student’s  $t$ -test should be utilized to calculate the sample variance. It is also to note that the errors of the velocity offsets given in parenthesis in Col.4, Table 2, range between 0.08 km  $\text{s}^{-1}$  and 0.7 km  $\text{s}^{-1}$ , whereas the velocity offset corresponding to  $\Delta F/F \sim 10^{-7}$  – the value set by the available limits on  $\Delta\mu/\mu$  cited in Sect. 1 – should be  $\sim 0.03$  km  $\text{s}^{-1}$ . Thus, the data are clearly noise-dominated. Then the errors of  $\Delta V$  cannot be used as weights in calculations of the sample mean and its variance because

<sup>2</sup> The Mopra radio telescope is part of the Australia Telescope which is funded by the Commonwealth of Australia for operation as a National Facility managed by CSIRO.

<sup>3</sup> This publication is based in part on data acquired with the Atacama Pathfinder Experiment (APEX). APEX is a collaboration between the Max-Planck-Institut für Radioastronomie, the European Southern Observatory, and the Onsala Space Observatory.

they are the errors of the noise amplitude and not the errors of the anticipated signal. That is why all statistical estimates are made with simple (unweighted) averaging of data points.

The velocity offset between lines of different elements is the sum of two components:

$$\Delta V = \Delta V_F + \Delta V_D, \quad (4)$$

where  $\Delta V_F$  is a regular velocity shift due to variation in  $F$ , and  $\Delta V_D$  is a random component caused by DN. Supposing a normally distributed DN and averaging over the total sample we obtain the mean value

$$\langle \Delta V \rangle = \langle \Delta V_F \rangle, \quad (5)$$

and the error of the mean

$$\sigma_{\langle \Delta V \rangle} = t_{p,\nu} \sigma_{\Delta V} / \sqrt{n}, \quad (6)$$

where  $n$  is the sample size, and  $t_{p,\nu}$  is the Student's  $t$ -test coefficient for the probability  $p = 0.7$  ( $1\sigma$ ) and the number of degrees of freedom  $\nu = 8$ .

The spectral lines CO(7–6) and [C I] are of *prime interest* to us since these transitions have nearby frequencies and were observed in the same band, i.e., simultaneously and with identical angular resolution (see Table 1). This eliminates part of the DN which can be caused by different beam filling factors for both emitting regions<sup>4</sup>. We note that different spatial morphologies and/or kinematic structure of the tracers within a single given beam size give rise to another part of DN which is of course not removed by such choice of lines.

The mean,  $\langle \Delta V \rangle$ , and the standard deviation,  $\sigma_{\Delta V}$ , of the velocity offsets between the  $n = 9$  pairs of CO(7–6) and [C I] lines from the  $1.11 \text{ km s}^{-1}$  channel width data are  $\langle \Delta V \rangle = -0.02 \text{ km s}^{-1}$  and  $\sigma_{\Delta V} = 0.2 \text{ km s}^{-1}$ . The non-parametric estimates for the centre (median) and the dispersion ( $= 1.48MAD$ , Median Absolute Deviation) give  $\Delta V_{\text{med}} = -0.01 \text{ km s}^{-1}$  and  $\sigma_{\Delta V_{\text{med}}} = 0.3 \text{ km s}^{-1}$ . These estimates are robust against large deviations from the sample mean and are usually used to detect outliers. Since here  $\sigma_{\Delta V_{\text{med}}} > \sigma_{\Delta V}$ , the sample can be considered as homogeneous.

For comparison, averaging over the sample of offsets between the same fine structure line [C I] from the *Herschel* data and rotational lines CO(1–0) and CO(3–2) observed with other facilities and with lower/higher angular resolutions, respectively, we obtain for the [C I]/CO(1–0) pair  $\langle \Delta V \rangle = -0.09 \pm 0.3 \text{ km s}^{-1}$  and for [C I]/CO(3–2)  $\langle \Delta V \rangle = -0.003 \pm 0.6 \text{ km s}^{-1}$ , i.e., as expected, these estimates are noticeably more dispersed. Taking this into account, all conclusions below refer to the measurements on the base of [C I]/CO(7–6).

The use of the [C II] line is less favorable than of [C I] since [C II] typically shows wider line profiles or additional velocity components whereas the [C I] and CO profiles are usually similar (Okada et al. 2019). This agrees with the result of Pineda et al. (2017) that  $\text{C}^+$  is the dominant gas-phase form of carbon associated with photodissociation regions (PDRs) – neutral regions where chemistry and heating are regulated by the far-UV photons (Hollenbach & Tielens

1999). Photons with energy  $E > 11.1 \text{ eV}$  dissociate CO into atomic carbon and oxygen in PDRs. Since the  $\text{C}^0$  ionization potential of  $11.3 \text{ eV}$  is quite close to the CO dissociation energy, neutral carbon can be quickly ionized. This suggests the chemical stratification of the PDR in a row  $\text{C}^+/\text{C}^0/\text{CO}$  with increasing depth from the surface of the PDR. That is why  $\text{C}^0$  and CO represent only a small fraction of PDRs, namely that where neutral gas is well shielded from the far-UV photons.

For instance, in our dataset wider and complex [C II] profiles with additional velocity components are observed practically in all systems, with SK-66D35 (Fig. 2) being the most evident case where the peak of the [C II] emission is shifted by  $\sim 3 - 4 \text{ km s}^{-1}$  with respect to the other lines (see Table 2)<sup>5</sup>. In the present work we use the [C II] as well as low- $J$  CO lines only to constrain the kinematic structure within the molecular clouds.

Now return to our sample of velocity offsets  $\Delta V$  between [C I] and CO(7–6) lines. In spite of its smallness, the sample is consistent with a normal distribution on formal criteria (sample values of the mean absolute deviation, asymmetry and kurtosis are well within  $1\sigma$  limits for a normal distribution). This allows us to calculate the mean and the error of the mean as given in (5, 6):  $\langle \Delta V \rangle = -0.02 \pm 0.07 \text{ km s}^{-1}$ . The systematic error due to uncertainties in the laboratory frequencies is almost an order of magnitude lower, so that the value of  $0.07 \text{ km s}^{-1}$  can be considered as the total measurement error<sup>6</sup>. Being expressed in terms of  $\Delta F/F$ , this error restricts the variability of  $F$  at the level  $|\Delta F/F| < 2 \times 10^{-7}$ .

For one target in the LMC – PDR3-NE – apart from measurements with a channel size of  $\Delta_{\text{ch}} = 1.11 \text{ km s}^{-1}$  common for all targets, there are also measurements of the [C I] and CO(7–6) lines with  $\Delta_{\text{ch}} = 0.19 \text{ km s}^{-1}$  (see Table 2). Such a high spectral resolution makes it possible to calculate the line centres with a statistical error of only  $0.01 - 0.02 \text{ km s}^{-1}$ . For the velocity offset we get in this case  $\Delta V = -0.05 \pm 0.02 \text{ km s}^{-1}$  and, correspondingly,  $|\Delta F/F| = (-1.7 \pm 0.7) \times 10^{-7}$ . Although consistent with the overall  $\Delta V$  estimate, here the negative offset becomes statistically significant. This target is located at the projected distance of about 4 kpc from the LMC centre, i.e., it falls in the region where DM dominates in the mass budget. Unfortunately, with the present data we cannot deduce whether this offset is entirely (or partly) caused by variations in  $F$  or indeed by different velocity fields in the CO and [C I] emitting regions. Namely, the [C I] and [C II] line centres taken with the *Herschel Space Observatory* coincide within the  $1\sigma$  uncertainty interval in spite of the differences in the angular resolutions and the line profile shapes. This can be interpreted as a cloud with a very compact and homogeneous core – as already was discussed above, generally [C II] emitting regions are much larger in size than those of [C I] and, hence, their velocity centroids may diverge. On the other

<sup>4</sup> At the LMC and SMC distances  $\theta = 1''$  correspond to  $R \simeq 0.2 - 0.3 \text{ pc}$ .

<sup>5</sup> Pineda et al. (2017) consider the [C II] and [C I]/CO emission as arising from two different sources SK-66D35-1 and SK-66D35-2.

<sup>6</sup> For comparison, the weighted mean and the standard deviation for the same sample (weights calculated as inverse squares of errors) are  $\langle \Delta V \rangle = -0.05 \text{ km s}^{-1}$  and  $\sigma_{\Delta V} = 0.12 \text{ km s}^{-1}$ . This demonstrates that the weighted standard deviation is underestimated.

hand, the centres of the rotational CO lines observed with other facilities show a large scatter (e.g., the offset  $\Delta V \simeq 1.1$  km s<sup>-1</sup> between CO(3–2) and CO(7–6) observed with similar resolution,  $\Delta_{\text{ch}} \simeq 0.2$  km s<sup>-1</sup>, Table 2) which hardly can be explained. Clearly, the kinematic structure of this perspective target should be studied in more detail.

Assuming that the variations in  $\mu$  may exceed those of  $\alpha$  (see, e.g., Langacker et al. 2002; Flambaum 2007; Uzan 2011; Brax 2014), we can transfer the obtained limits on  $\Delta F/F$  to  $\Delta\mu/\mu$ . A sign of  $\Delta\mu/\mu$  is expected to be negative since the additional coupling of the hypothetical non-standard field(s) to baryonic matter may increase the mass of the electron  $m_e$ , whereas the proton mass  $m_p$ , being determined mostly by the binding energy of quarks, remains practically unchanged.

It is interesting to compare the values of  $\Delta\mu/\mu$  measured in the Magellanic Clouds where the overall mass budget is dominated by DM with values from objects with different ratios of baryonic matter to DM. As was already mentioned above, baryons are supposed to constitute about 90% of the dynamical mass at the position of the Sun. For several nearby molecular cores (detached by  $\lesssim 300$  pc) the estimates of  $\Delta\mu/\mu$  were obtained in the framework of a program to test the chameleon screening. Strange enough, but in all measurements a negative  $\Delta\mu/\mu$  of a few  $10^{-8}$  was reproduced in spite of using a variety of molecular transitions and observing with different radio telescopes (Levshakov et al. 2010a,c; Daprà et al. 2017). However,  $10^{-8}$  is just the level of the systematic error which in the present case comprises both the limiting accuracy of the observing facilities and the uncertainty in the laboratory frequencies of the employed molecular transitions (Levshakov et al. 2013). Thus, these results allow us to set only an upper limit on possible changes in  $\mu$  in media where baryonic matter dominates:  $|\Delta\mu/\mu| < 3 \times 10^{-8}$ .

There is one estimate of a comparable accuracy reported for an absorption system at  $z = 0.89$ :  $\Delta\mu/\mu = (-3.0 \pm 6.0) \times 10^{-8}$  (Kanekar et al. 2015; Marshall et al. 2017). The estimate was obtained with different transitions of the same molecule CH<sub>3</sub>OH, i.e., the influence of the DN and chemical segregation is minimal in this case. The system probably originates in a spiral arm at a distance of  $\sim 2$  kpc from the centre of a massive spiral galaxy (Muller et al. 2006). As expected, the limit on  $\Delta\mu/\mu$  in the  $z = 0.89$  system complies with that for the MW disk.

On the other hand, Kanekar (2011) reports  $\Delta\mu/\mu = (-3.5 \pm 1.2) \times 10^{-7}$  measured on base of NH<sub>3</sub>, CS and H<sub>2</sub>CO molecular lines detected in a  $z = 0.69$  absorber. These absorption lines arise in the halo of a low luminosity dwarf galaxy and deep image observations do not reveal any neighboring galaxy at the projected distance less than 65 kpc (Falomo et al. 2017), i.e., this system resembles the objects in the Magellanic Clouds. However, the velocity offset between the above combination of molecules can contain a significant input from DN – just as it is observed between the [C I] and CO transitions used in our study. To estimate and to eliminate the influence of DN, new measurements employing a complete palette of suitable transitions are required.

## 5 SUMMARY AND FUTURE PROSPECTS

We have used high resolution submillimeter spectra of the [C I], [C II] and CO emission lines from objects in the Magellanic Clouds to measure the velocity shifts between molecular rotational lines and atomic fine structure lines. Such shifts can be (partly) attributed to the variations in the fundamental constants  $\mu$  and  $\alpha$  which in turn can be caused by coupling of the non-standard fields to ordinary matter. The overall mass budget in the Magellanic Clouds is dominated by DM, thus making them to be favourable targets to search for manifestations of such fields.

Using the *Herschel Space Observatory* observations of CO(7–6) 806.5 GHz and [C I] 809.3 GHz transitions from nine molecular clouds in both the LMC and SMC and averaging over the whole sample we obtained  $\langle \Delta V \rangle = -0.02 \pm 0.07$  km s<sup>-1</sup> or, in terms of  $\Delta F/F$ ,  $\Delta F/F = (-0.7 \pm 2.3) \times 10^{-7}$ , where  $F = \mu\alpha^2$ . However, for one object where the observations were carried out with a 5 times better spectral resolution, the result was  $\Delta V = -0.05 \pm 0.02$  km s<sup>-1</sup> and, correspondingly,  $\Delta F/F = (-1.7 \pm 0.7) \times 10^{-7}$ .

Before attributing the measured velocity shifts entirely (or partly) to changes in the fundamental constants one has to exclude velocity components arising from the kinematic structure of the observed clouds.

This can be done in different ways. One possibility is to study the gas velocity distribution in greatest detail by involving other molecules. For instance, CH is an intermediate molecule in gas-phase chemical reactions from C to CO and, thus, its emission traces their common spatial distribution (Sakai et al. 2012). The fundamental spin-rotational transitions of CH at 533 GHz and 537 GHz have already been considered as probes for a possible variation of coupling constants (de Nijs et al. 2012). Other CH transitions at lower frequencies 3.3 GHz and 0.7 GHz were discussed for the same tasks in Kozlov (2009) and Truppe et al. (2013). Another important intermediate molecule for the production of CO is OH (Sakai et al. 2012) which also can be used for mapping the velocity field in molecular clouds.

The second possibility is to use different transitions of the same molecule. As is known, the methanol molecule has a complex microwave spectrum with a large number of very strong lines which have different sensitivity to  $\mu$ -variations (Jansen et al. 2011; Levshakov et al. 2011). Recent detections of methanol (CH<sub>3</sub>OH) in the LMC (Sewiło et al. 2018) and SMC (Shimonishi et al. 2018) make this possibility a very promising option.

Most proposed molecular transitions fall in the frequency range covered by ALMA bands. It is to expect that future observations with this telescope as well as new laboratory measurements of the rest frequencies of perspective transitions will help to reduce significantly the systematic errors and, hence, to answer the question whether additional coupling due to non-standard fields is indeed present or not.

## ACKNOWLEDGMENTS

We thank the anonymous referee for critical reading of the manuscript. The work of S.A.L. was partially supported by the Russian Science Foundation under grant No. 19-12-00157.

## REFERENCES

- Agafonova I. I., Molaro P., Levshakov S. A., Hou J. L., 2011, *A&A*, 529, A28
- Antoniou I., Perivolaropoulos L., 2017, *PhRvD*, 96, 1040002
- Archibald A. M., Gusinskaia N. V., Hessels J. W. T., Deller A. T., Kaplan D. L., Lorimer D. R., Lynch R. S., Ransom S. M., Stairs I. H., 2018, *Nature*, 559, 73
- Bainbridge M. B., Webb J. K., 2017, *MNRAS*, 468, 1639
- Berezhiani L., Khoury J., 2015, *PhRvD*, 95, 043541
- Bergé J., Brax P., Métris G., Pernot-Borràs M., Touboul P., Uzan J.-P., 2018, *PhRvL*, 120, 141101
- Brax P., 2018, *RPPH*, 81, 016902
- Brax P., 2014, *PhRvD*, 90, 023505
- Brax P., Davis A.-C., 2016, *PhRvD*, 94, 104069
- Buckley M. R., Charles E., Gaskins J. M., Brooks A. M., Drlica-Wagner A., et al. 2015, *PhRD*, 91, 102001
- Cooksy A. L., Blake G. A., Saykally R. J., 1986, *ApJ*, 305, L89
- Daprà M., Henkel C., Levshakov S. A., Menten K. M., Muller S., et al., 2017, *MNRAS*, 472, 4434
- de Graauw Th., Helmich F. P., Phillips T. G., Stutzki J., Caux E., Whyborn N. D., Dieleman P., et al. 2010, *A&A*, 518, L6
- de Nijs A. J., Ubachs W., Bethlem H. L., 2012, *PRA*, 86, 032501
- Di Teodoro E. M., McClure-Griffiths N. M., Jameson K. E., Dénes H., Dickey J. M., et al., 2019, *MNRAS*, 483, 392
- Endres C. P., Schlemmer S., Schilke P., Stutzki J., Müller H. S. P., 2016, *J. Mol. Spectrosc.*, 327, 95
- Falomo R., Treves A., Scarpa R., Paiano S., Landoni M., 2017, *MNRAS*, 470, 2814
- Feng J. L., 2010, *ARA&A*, 48, 495
- Flambaum V. V., 2007, *Int. J. Mod. Phys. A*, 22, 4937
- Gupta N., Momjian E., Srianand R., Petitjean P., Noterdaeme P., Gyanchandani D., Sharma R., Kullkarni S., 2018, *ApJL*, 860, L22
- Hamilton P., Jaffe M., Haslinger P., Simmons Q., Müller H., Khoury J., 2015, *Science*, 349, 849
- Haris K., Kramida A., 2017, *ApJS*, 233, 16
- Hollenbach D. J., Tielens A. G. G., 1999, *Rev. Mod. Phys.*, 71, 173
- Hui L., Ostriker J., Tremaine S., Witten E., 2017, *PhRvD*, 95, 043541
- Iocco, F., Pato M., Bertone G., 2015, *NPhys.*, 11, 245-248
- Irastorza I. G., Redondo J., 2018, *PrPNP*, 102, 89
- Jansen P., Xu L.-H., Kleiner I., Ubachs W., Bethlem H. L., 2011, *PRL*, 106, 100801
- Joyce A., Lombriser L., Schmidt F., 2016, *ARNPS*, 66, 95.
- Kanekar N., 2011, *ApJ*, 728, L12
- Kanekar N., Ghosh T., Chengalur J. N., 2018, *PRL*, 120, 061302
- Kanekar N., Ubachs W., Menten K. M., Bagdonaite J., Brunthaler A., et al., 2015, *MNRAS*, 448, L104
- Khoury J., Weltman A., 2004, *PhRvL*, 93, 171104
- Kotuš S. M., Murphy M. T., Carsell R. F., 2017, *MNRAS*, 464, 3679
- Kozlov M. G., 2009, *PRA*, 80, 022118
- Kozlov M. G., Safronova M. S., Crespo López-Urrutia J. R., Schmidt P. O., 2018, *RvMP*, 90, 045005
- Kozlov M. G., Levshakov S. A., 2013, *Ann. Phys.*, 525, 452
- Langacker P., Segrè G., Schilke P., Strassler J., 2002, *Phys. Lett. B*, 528, 121
- Levshakov S. A., Ng K.-W., Henkel C., Mookerjee B., 2017, *MNRAS*, 471, 2143
- Levshakov S. A., Reimers D., Henkel C., Winkel B., Mignano A., Centurión M., Molaro P., 2013, *A&A*, 559, A91
- Levshakov S. A., Kozlov M. G., Reimers D., 2011, *ApJ*, 738, 26
- Levshakov S. A., Lapinov A. V., Henkel C., Molaro P., Reimers D., Kozlov M. G., Agafonova I. I., 2010a, *A&A*, 524, A32
- Levshakov S. A., Molaro P., Reimers D., 2010b, *A&A*, 516, A113
- Levshakov S. A., Molaro P., Lapinov A. V., Reimers D., Henkel C., Sakai T., 2010c, *A&A*, 512, A44
- Levshakov S. A., Reimers D., Kozlov M. G., Porsev S. G., Molaro P., 2008, *A&A*, 479, 719
- Levshakov S. A., Centurión M., Molaro P., D’Odorico S., Reimers D., et al., 2006, *A&A*, 449, 879
- Li K., Arif M., Cory D. G., Haun R., Heacock B., Huber M. G., Nsofini J., et al., 2016, *PhRvD*, 93, 062001
- Marshall M. A., Ellingsen S. P., Lovell J. E. J., Dickey J. M., Voronkov M. A., Breen S. L., 2017, *MNRAS*, 466, 2450
- McGaugh S. S., 2018, *RNAAS*, 2, 37
- McMillan P. J., 2017, *MNRAS*, 465, 76
- Molaro P., Centurión M., Whitmore J. B., Evans T. M., Murphy M. T., Agafonova I. I., Bonifacio P., et al., 2013, *A&A*, 555, A68
- Muller S., Guélin M., Dumke M., Lucas R., Combes F., 2006, *A&A*, 458, 417
- Nojiri S., Odintsov S. D., Oikonomou V. K., 2017, *PhR*, 692, 1
- Okada Y., Güsten R., Requena-Torres M. A., Röllig M., Stutzki J., Graf U. U., Hughes A., 2019, *A&A*, 621, A62
- Pilbratt G. L., Riedinger J. R., Passvogel T., Crone G., Doyle D., Gageur U., Heras A. M., et al. 2010, *A&A*, 518, L1
- Pineda J. L., Langer W. D., Goldsmith P. F., Horiuchi S., Kuiper T. B. H., Muller E., Hughes A., et al., 2017, *ApJ*, 839, 107
- Quast R., Reimers D., Levshakov S. A., 2004, *A&A*, 415, L7
- Rider A. D., Moore D. C., Blakemore C. P., Louis M., Lu M., Gratta G., 2016, *PhRvL*, 117, 101101
- Safronova M. S., Budker D., DeMille D., Kimball D. F. J., Derevianko A., Clark C. W., 2018, *RvMP*, 90, 025008
- Sakai N., Maezawa H., Sakai T., Menten K. M., Yamamoto S., 2012, *A&A*, 546, A103
- Savitzky A., Golay M. J. E., 1964, *Anal. Chem.*, 36, 1627
- Sewilo M., Indebetouw R., Charnley S. B., Zahorecz S., Oliveria J. M., van Loon J. Th., Ward J. L., et al., 2018, *ApJL*, 853, L19
- Shimonishi T., Watanabe Y., Nishimura Y., Aikawa Y., Yamamoto S., Onaka T., Sakai N., Kawamura A., 2018, *ApJ*, 862, 102
- Sofue Y., Honma M., Omodaka T., 2009, *PASJ*, 61, 227
- Truppe S., Hendricks R. J., Tokunaga S. K., Lewandowski H. J., Kozlov M. G., Henkel C., Hinds E. A., Tarbutt M. R., 2013, *NComms*, 4, 2600
- Ubachs W., 2018, *SSR*, 214, 3
- Uzan J.-P., 2011, *LRR*, 14, 2
- van der Marel R. P., Kallivayalil N., 2014, *ApJ*, 781, 121
- Vasiliev E., 2018, *MNRAS*, 481, L100
- Verlinde E., 2017, *ScPP*, 2, 016
- Wagner T. A., Schlamming S., Gundlach J. H., Adelberger E. G., 2012, *Class. Quantum Grav.*, 29, 184002
- Will C. H., 2014, *LRR*, 17, 4

This paper has been typeset from a  $\text{\TeX}/\text{\LaTeX}$  file prepared by the author.

**Table 1.** The atomic and molecular transitions used in the present study. Column 2 shows laboratory frequencies and their uncertainties taken from the cited in the last column papers. The corresponding systematic errors in velocity are given in Column 3. Column 4 lists beamsizes of the observations.

Transition	Frequency (GHz)	$\sigma_{\text{sys}}$ (km s <sup>-1</sup> )	$\theta_{\text{obs}}$ (arcsec)	Reference
[C I] <sup>3</sup> P <sub>2</sub> - <sup>3</sup> P <sub>1</sub>	809.341970(17)	0.006	26.5	Haris & Kramida (2017)
CO(7-6)	806.65180600(50)	0.0019	26.5	Endres et al. (2016)
[C II] <sup>2</sup> P <sub>3/2</sub> - <sup>2</sup> P <sub>1/2</sub>	1900.5369(13)	0.205	12.0	Cooksy et al. (1986)
CO(1-0)	115.27120180(50)	0.0013	33.0	Endres et al. (2016)
CO(3-2)	345.79598990(50)	0.0004	17.5	Endres et al. (2016)

**Table 2.** Radial velocities  $V_{\text{LSR}}$  of the CO rotational lines ( $V_{\text{rot}}$ ) and the [C I], [C II] fine structure lines ( $V_{\text{fs}}$ ) measured in molecular clouds in the LMC and SMC.  $\Delta V$  is the velocity offset between the CO(7-6) and [C I] lines. The data were obtained with: [C I], CO(7-6), and [C II] – the *Herschel Space Observatory*, wherein [C I] and CO(7-6) were observed simultaneously within the same band; CO(1-0) – the *Australia Telescope National Facility (ATNF) Mopra Telescope*; CO(3-2) – the *Atacama Pathfinder Experiment (APEX) Telescope*. The channel widths used: (a) 0.88 km s<sup>-1</sup>, (b) 1.11 km s<sup>-1</sup>, (c) 0.19 km s<sup>-1</sup>, (d) 0.79 km s<sup>-1</sup>, (e) 1.00 km s<sup>-1</sup>, (f) 0.17 km s<sup>-1</sup>, (g) 0.69 km s<sup>-1</sup>, (h) 0.70 km s<sup>-1</sup>, (i) 1.04 km s<sup>-1</sup>. The numbers in parentheses correspond to  $1\sigma$  statistical errors on the last digits.

LOSs	CO(7-6) $V_{\text{LSR}}$ , km s <sup>-1</sup>	[C I] <sup>3</sup> P <sub>2</sub> - <sup>3</sup> P <sub>1</sub> $V_{\text{LSR}}$ , km s <sup>-1</sup>	$\Delta V =$ $V_{\text{rot}} - V_{\text{fs}}$ , km s <sup>-1</sup>	CO(1-0) $V_{\text{LSR}}$ , km s <sup>-1</sup>	CO(3-2) $V_{\text{LSR}}$ , km s <sup>-1</sup>	[C II] <sup>2</sup> P <sub>3/2</sub> - <sup>2</sup> P <sub>1/2</sub> $V_{\text{LSR}}$ , km s <sup>-1</sup>
(1)	(2)	(3)	(4)	(5)	(6)	(7)
<i>Large Magellanic Clouds</i>						
PDR3-NE	271.81(2) <sup>b</sup> 271.81(1) <sup>c</sup>	271.85(8) <sup>b</sup> 271.86(2) <sup>c</sup>	-0.04(8) -0.05(2)	271.96(6) <sup>a</sup>	272.88(2) <sup>f</sup>	271.85(7) <sup>d</sup>
SK-66D35	276.8(4) <sup>b</sup>	276.8(2) <sup>b</sup>	0.0(4)	276.2(2) <sup>a</sup>	275.90(9) <sup>e</sup>	280.0(3) <sup>d</sup>
LMC2-NW	288.7(7) <sup>b</sup>	288.55(9) <sup>b</sup>	0.2(7)	288.92(7) <sup>a</sup>		
NT77	217.60(10) <sup>b</sup>	217.9(2) <sup>b</sup>	-0.3(2)	218.00(4) <sup>a</sup>	217.90(8) <sup>f</sup>	217.38(5) <sup>d</sup>
<i>Small Magellanic Clouds</i>						
SMC-NE-3g	169.3(3) <sup>b</sup>	169.1(3) <sup>b</sup>	0.2(4)	168.99(4) <sup>h</sup>	169.2(3) <sup>i</sup>	169.1(3) <sup>d</sup>
SMC-NE-1a	149.18(16) <sup>b</sup>	149.30(16) <sup>b</sup>	-0.1(2)	148.88(4) <sup>h</sup>	148.8(6) <sup>g</sup>	148.93(13) <sup>d</sup>
SMC-B2-6	120.8(2) <sup>b</sup>	120.56(13) <sup>b</sup>	0.2(2)	120.55(5) <sup>a</sup>	120.1(2) <sup>g</sup>	121.01(8) <sup>d</sup>
SMC-LIRS36	126.29(6) <sup>b</sup>	126.30(7) <sup>b</sup>	-0.01(10)	126.29(4) <sup>a</sup>	126.41(8) <sup>g</sup>	126.49(7) <sup>d</sup>
SMC-LIRS49	114.4(2) <sup>b</sup>	114.68(5) <sup>b</sup>	-0.3(2)	114.44(19) <sup>a</sup>	114.50(17) <sup>g</sup>	114.98(16) <sup>d</sup>

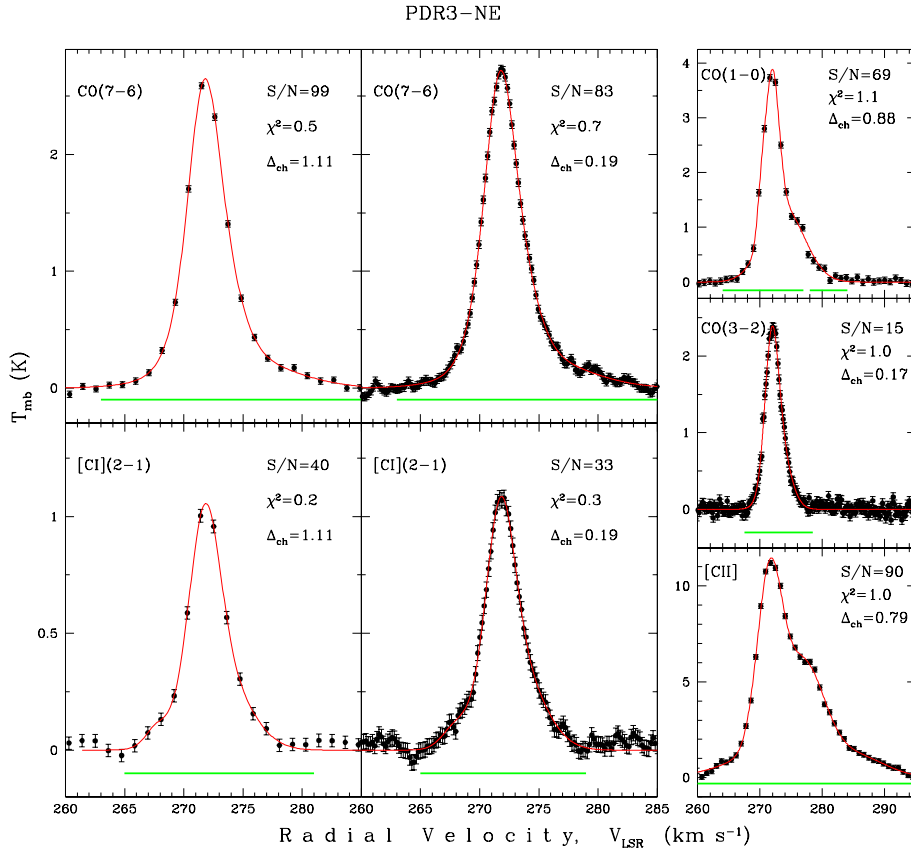


**Figure 1.** Observed spectra (dots with  $1\sigma$  error bars) towards the molecular cloud PDR3-NE in the LMC (see Table 1). Radial velocities are given in km s<sup>-1</sup> relative to the Local Standard of Rest (LSR) and the line intensities are in units of the telescope mean beam temperature  $T_{\text{mb}}$  (K). For each spectrum the signal-to-noise ratio (S/N) per channel at the maximum intensity peak,  $\chi^2$  per degree of freedom, and the channel width  $\Delta_{\text{ch}}$  (in km s<sup>-1</sup>) are indicated. The fitting curves are shown by red. The horizontal green lines mark spectral ranges included in the fitting procedure.



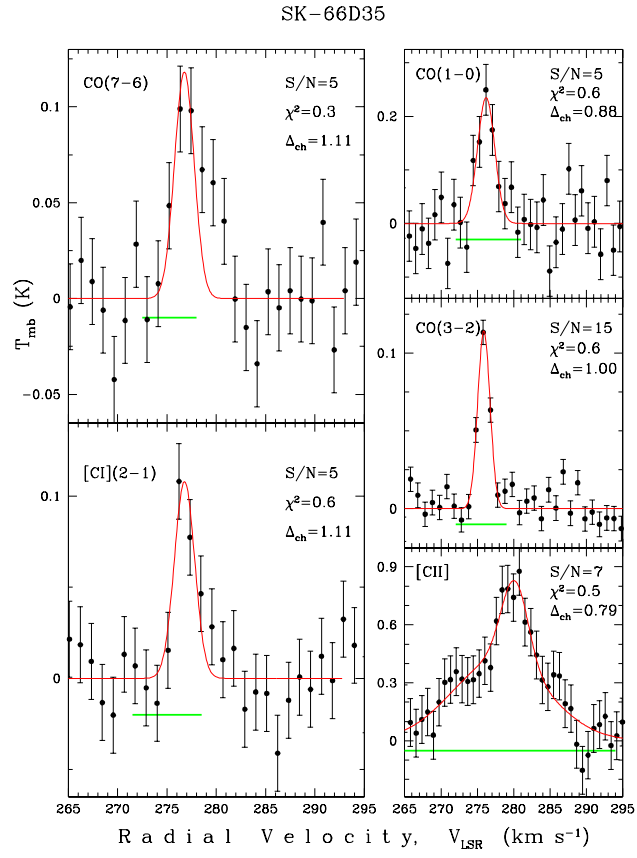


**Figure 2.** Same as Fig. 1, but for the molecular cloud SK-66D35 in the LMC.

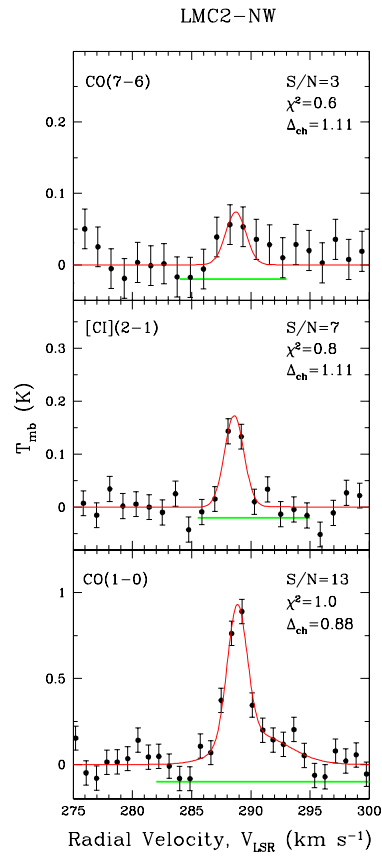


**Figure 3.** Same as Fig. 1, but for the molecular cloud LMC2-NW in the LMC.

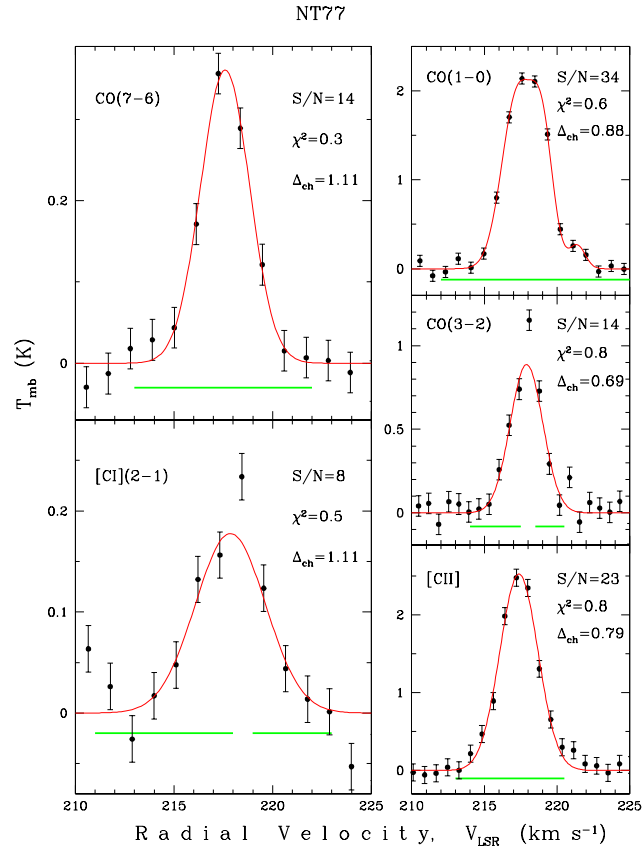


**Figure 4.** Same as Fig. 1, but for the molecular clouds NT77 in the LMC.

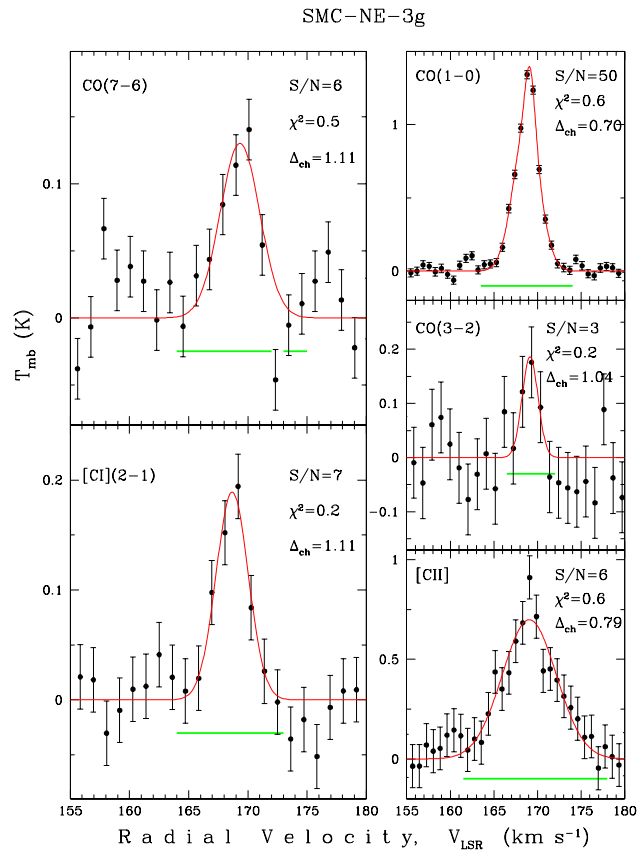


**Figure 5.** Same as Fig. 1, but for the molecular cloud SMC-NE-3g in the SMC.

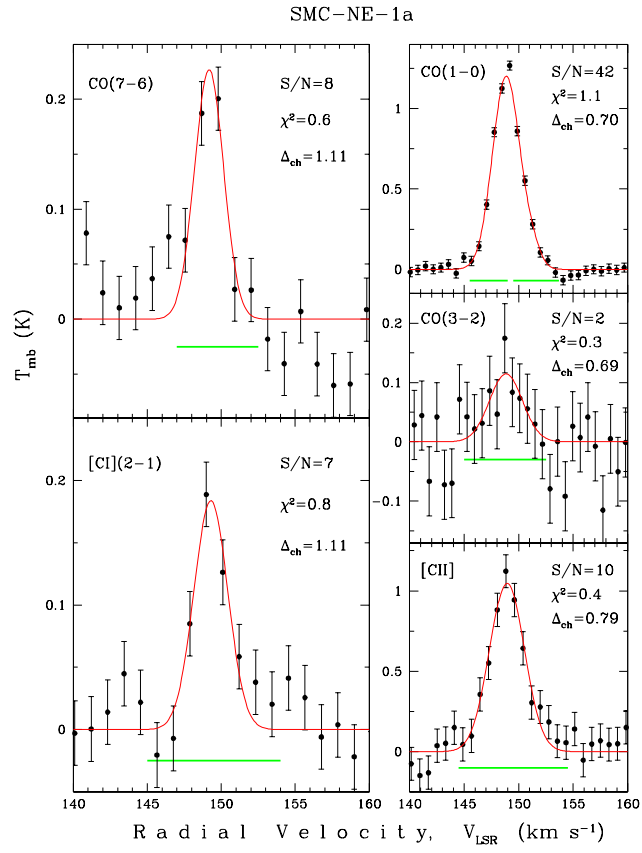
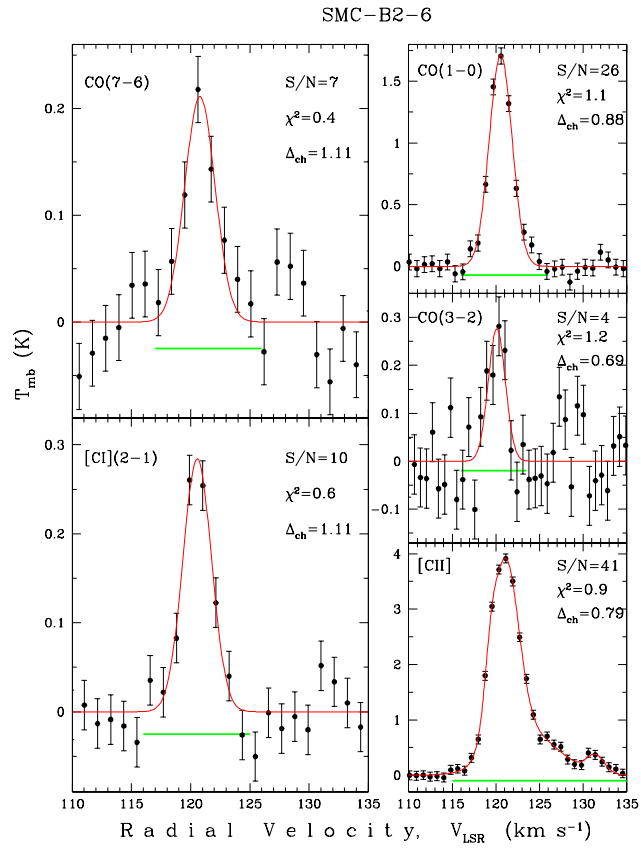


Figure 6. Same as Fig. 1, but for the molecular cloud SMC-NE-1a the SMC.



**Figure 7.** Same as Fig. 1, but for the molecular cloud SMC-B2-6 in the SMC.

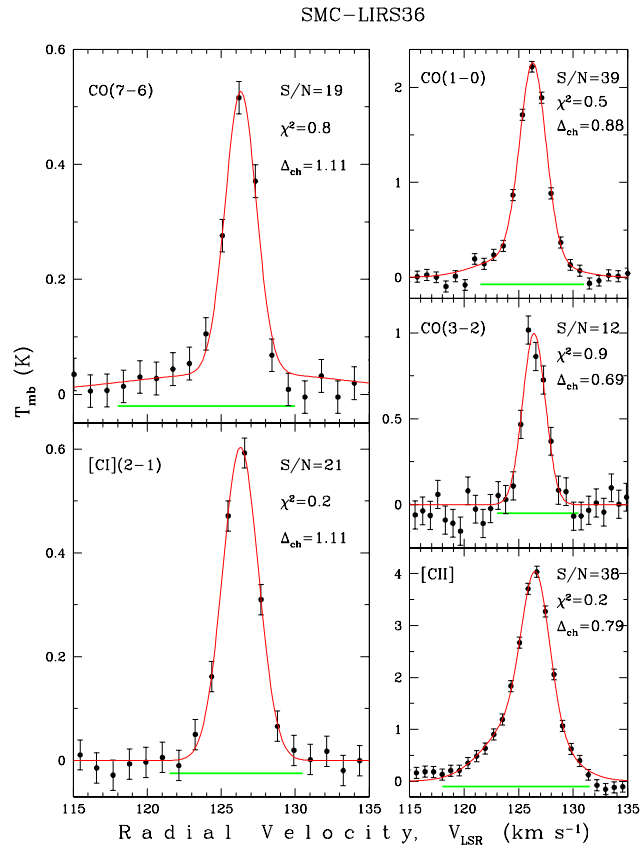
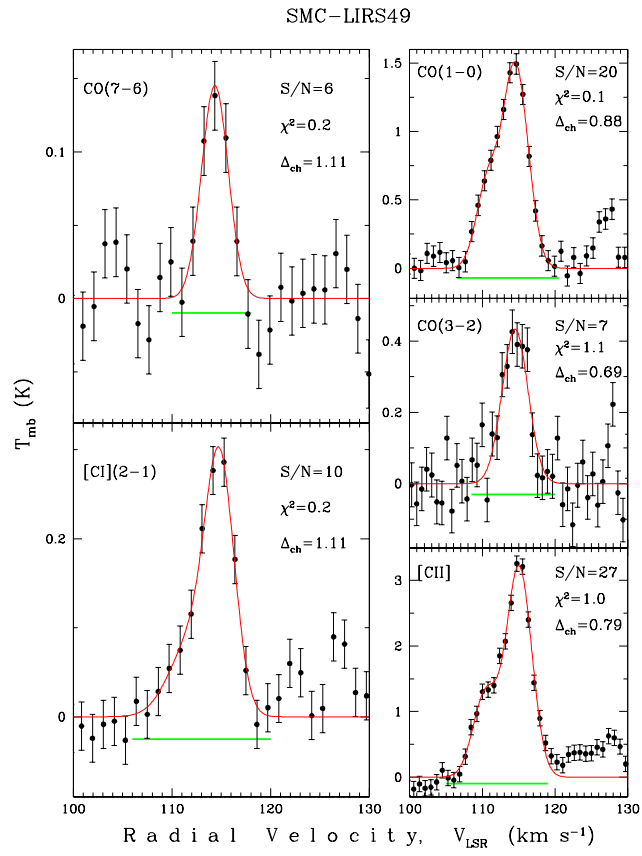


Figure 8. Same as Fig. 1, but for the molecular cloud SMC-LIRS36 in the SMC.



**Figure 9.** Same as Fig. 1, but for the molecular cloud SMC-LIRS49 in the SMC.